Reaction Chemistry & Engineering

ROYAL SOCIETY OF CHEMISTRY

PAPER

View Article Online
View Journal | View Issue

Cite this: *React. Chem. Eng.*, 2024, **9**, 2902

Kinetics of thermal dry reforming of methane for syngas production and solid carbon capture†

Manas Mokashi,[a] Akash Bhimrao Shirsath,[a] Sinan Demir,[a] Ahmet Çelik,[a] Patrick Lott,*[a] Steffen Tischer[b] and Olaf Deutschmann[ab]

Received 28th June 2024,
Accepted 6th August 2024

DOI: 10.1039/d4re00312h

rsc.li/reaction-engineering

Dry reforming of CH_4, either by co-feeding CH_4 and CO_2 from waste streams or directly using biogas, has potential as a CO_2-sink. This study investigates entirely thermal, catalyst-free dry reforming in a tubular flow reactor, aiming for syngas production with concurrent carbon capture. Kinetic modelling couples an elementary step-based gas-phase mechanism with a carbon deposition model. One-dimensional numerical simulations of the flow reactor are compared with experimental measurements. For this, operating conditions are widely varied, in particular temperature (1273 K to 1873 K), residence time (1 to 7 seconds), and CH_4 : CO_2 molar feed ratio (1 to 4). Two temperature regimes are identified, with varying dominance of the reverse water-gas shift and CH_4 pyrolysis reactions. Above 1673 K, CO_2 is fully consumed, independent of residence time and feed composition. Optimized operating parameters result in a H_2/CO ratio of 2 in the effluent gas stream, *e.g.* as commonly desired for methanol and oxo-alcohol synthesis. Notably, under such optimized conditions, only a minor share of carbonaceous species remains in the gas-phase as hydrocarbons, while 33% of the CH_4-borne carbon is transformed into CO and 48% of CH_4-borne carbon is captured as solid carbon.

Introduction

In the context of reducing greenhouse gas emissions, hydrogen (H_2) is projected to play a pivotal role as a carbon-free energy carrier.[1,2] It is also essential for carbon capture and utilization (CCU) technologies such as direct hydrogenation of carbon dioxide (CO_2) into methanol[3–5] and olefins.[6,7] However, with regard to large-scale production of H_2 that is necessary to cover the increasing demand, the entirely carbon-free production process through water electrolysis faces challenges such as high initial investment costs and substantial energy requirements.[8,9] Therefore, methane (CH_4) pyrolysis is gaining increasing attention as a bridging technology for H_2 production on the pathway towards a sustainable future.[10–14] This endothermic process that does not exhibit any direct CO_2 emissions involves the decomposition of CH_4, resulting in the production of H_2 and the capture of solid carbon[2,10] according to eqn (1).

$$CH_4 \rightarrow 2H_2 + C \quad \Delta_R H^\circ = 75 \text{ kJ mol}^{-1} \tag{1}$$

Since, H_2 is of high relevance as a raw material within the chemical industry,[15] particular focus has been laid on the direct conversion of natural gas with its main component CH_4 into H_2, carbon monoxide (CO), and olefins.[16–19] To date, one of the most frequently chosen industrial approaches is the indirect conversion of CH_4 into value-added chemicals *via* syngas, a mixture of H_2 and CO, owing to its enhanced efficiency and versatility.[20,21] Syngas can be utilized in various processes, including methanol synthesis, olefins production *via* methanol and dimethyl-ether intermediates, Fischer–Tropsch synthesis for fuel production, and oxo-alcohol synthesis.[22] Among the technologies employed for syngas production, processes relying on a catalyst are typically the premier choice, in particular steam methane reforming (SMR),[23] autothermal reforming (ATR),[24] partial oxidation (POX),[25,26] and dry reforming of methane (DRM).[22,27–29] Among these processes, DRM according to eqn (2) stands out for its remarkable potential in directly valorizing CO_2 as a feedstock.[22]

$$CH_4 + CO_2 \rightleftharpoons 2CO + 2H_2 \quad \Delta_R H^\circ = 247 \text{ kJ mol}^{-1} \tag{2}$$

In the future, CH_4 obtained from fossil sources is expected to be substituted with biogas originating from renewable feedstocks. Biogas, a blend of CH_4 and CO_2,[30] is well-suited for direct use in the DRM process. Additionally, CO_2 captured from heavy industries and CH_4 can be co-fed into the DRM reactor, which enhances its potential as a large-scale CO_2-

[a] *Institute for Chemical Technology and Polymer Chemistry, Karlsruhe Institute of Technology (KIT), Engesserstr. 20, 76131 Karlsruhe, Germany.*
E-mail: patrick.lott@kit.edu
[b] *Institute of Catalysis Research, Karlsruhe Institute of Technology (KIT), Hermann-von-Helmholtz-Platz 1, 76344 Eggenstein-Leopoldshafen, Germany*

† Electronic supplementary information (ESI) available: Details on mechanism and additional data on by-products. See DOI: https://doi.org/10.1039/d4re00312h

negative technology. In order to activate the rather stable molecules CH_4 and CO_2, catalytic systems containing noble metals such as Pd, Pt, Rh, and Ru have been studied extensively.[31–34] However, their high price impedes their industrial implementation. Due to their significantly lower price and fairly high activity, also Ni-based catalysts are considered promising.[35–39] Similarly, Co-based catalysts were subject to research, mainly due to the cost advantage over noble metals, but their stability still remains a challenge.[40] Notably, the choice of decent metal oxide support materials such as Al_2O_3, MgO, CeO_2, SiO_2, La_2O_3, and ZrO_2, or the use of carbon nanotubes or transition metal carbides were reported to increase both the catalytic activity and long-term stability of non-noble metal-based catalyst formulations for dry reforming of CH_4.[41–44] Nonetheless, one of the primary challenges encountered in this process is the rapid catalyst deactivation due to coke formation.[22,29,45–47]

An alternative strategy to directly use CO_2 in chemical processes and circumvent the challenges associated with catalyst deactivation is through a non-catalytic high-temperature approach.[48–53] In this context, Angeli *et al.*[51] reported the utilization of steelwork off-gases through an entirely thermal DRM process and Blanck *et al.*[53] studied the influence of operating parameters for steelwork off-gases in a pilot plant. They found that 97% CH_4 conversion and 94% CO_2 conversion can be obtained at 1721 K. In addition to CH_4 and CO_2, steelwork off-gases contain high levels of CO, nitrogen (N_2), and water (H_2O). Furthermore, Chen and Gan[49] investigated non-catalytic thermal DRM in the presence of oxygen (O_2) and found that a feed ratio of CH_4, O_2, and CO_2 of 5 : 4 : 1 results in a conversion of 99.88% and 46.85% for CH_4 and CO_2, respectively, with the resulting syngas exhibiting a H_2/CO ratio of 1.19. Savchenko *et al.*[50] carried out a kinetic analysis of non-catalytic DRM involving C_1–C_4 hydrocarbons in a temperature range spanning from 1400 K to 1800 K. Their findings highlighted the central role played by acetylene (C_2H_2) in the non-catalytic DRM process.

In the context of entirely sustainable feedstocks, Shapovalova *et al.*[52] employed volumetric matrix reformers to transform biogas with a CO_2 content exceeding 60 mol% into syngas. Furthermore, Çelik *et al.*[48] conducted comprehensive experimental investigations on biogas pyrolysis in a flow reactor setup with a feed mixture of H_2-diluted CH_4/CO_2 mixtures for temperatures ranging from 1273 K to 1873 K, with residence times (τ) spanning from 1 to 7 seconds, and CH_4 : CO_2 molar feed ratios varying from 1 to 4. In addition to carbon deposition that enables the process to act as a carbon sink, syngas formation was observed, resulting in an essentially full exploitation of the feed gas stream.

Despite promising prior research efforts, profound mechanistic studies of syngas production and simultaneous capture of solid carbon in thermal, non-catalytic DRM lack so far. At the elevated temperatures necessary for thermal DRM, and with the presence of additional species such as CO_2 and H_2 in the feed, in addition to CH_4 pyrolysis the reverse water-gas shift reaction (RWGS) (eqn (3)) becomes relevant. It is important to note that the RWGS reaction is reversible; therefore, it is highly sensitive to changes of feed composition, temperature, and pressure.[54]

$$H_2 + CO_2 \rightleftharpoons CO + H_2O \quad \Delta_R H^\circ = 41 \text{ kJ mol}^{-1} \tag{3}$$

Overall, a fundamental knowledge on the interplay between methane pyrolysis, DRM, and RWGS that is mandatory for designing potential non-catalytic high-temperature processes, lacks to date. Thus, our current study bridges this gap by combining numerical simulations and experimental investigations of thermal, non-catalytic DRM using H_2-diluted mixtures of CH_4 and CO_2 as feed. For this, we coupled an elementary step-based gas-phase kinetic mechanism with a carbon deposition model, and the simulations are evaluated against experimental data. The impact of process parameters such as temperature, feed gas composition, and residence time is thoroughly investigated by analyzing axial profiles of the gas-phase species and deposited carbon. Herewith, we contribute to a more profound understanding of the high-temperature non-catalytic thermal DRM process and influence of operating conditions on both the gas-phase products as well as solid carbon formation.

Experimental

The experiments were performed in a high-temperature and high-pressure flow reactor setup that was already described in previous work.[10,51] The reactor consists of ceramic α-Al_2O_3 (DEGUSSIT AL23 by Friatec/Aliaxis) and has a length of 1 m and an inner diameter of 0.02 m. The reaction mixture was pre-heated to 443 K and fed to the reactor *via* mass flow controllers. The effluent products were analyzed with an online HPR-20 mass spectrometer (Hiden Analytical). The experimental setup is schematically illustrated in Fig. 1.

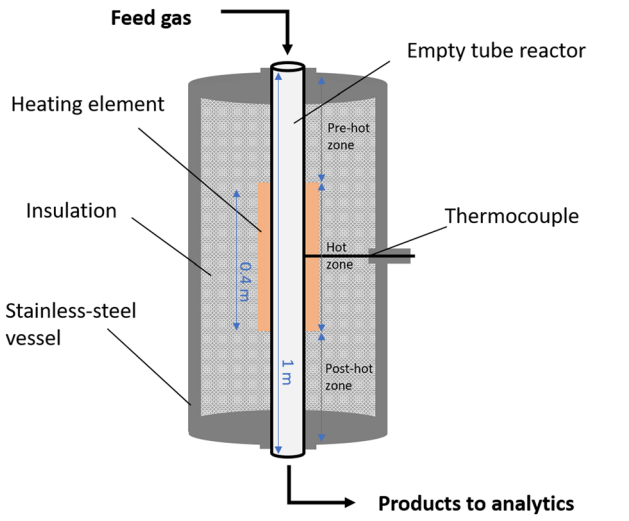

Fig. 1 Experimental flow reactor setup.

Table 1 Experimental operating conditions used for model evaluation

Process parameter	Variation range
Temperature/K	1273–1373–1473–1573–1673–1773–1873
Residence time/s	1–3–5–7
Pressure/bar	1

Table 2 Feed gas composition as molar fractions of each species in the experiments used for model evaluation

Molar feed ratio	CH_4	CO_2	H_2
$CH_4:CO_2$ ratio 1	0.167	0.167	0.667
$CH_4:CO_2$ ratio 2	0.222	0.111	0.667
$CH_4:CO_2$ ratio 4	0.2664	0.0666	0.667

The procedure for the experiments that serve for model validation and evaluation herein is based on the approach chosen during a recently published study by our group.[48] In particular, the reactor was operated under reaction conditions for 20 minutes while monitoring the composition of the effluent gas stream. Subsequently, any carbon deposited in the reactor was oxidized at temperatures above 1273 K in order to recover the reactor for the next experiment. The recovery was considered to be complete once the end-of-pipe CO and CO_2 levels reached zero. The operating conditions and inlet feed compositions used for model development and validation are summarized in Tables 1 and 2, respectively. Specific flow rates that were chosen during the experiments in order to achieve the desired residence times are provided in the supplementary material (Tables S1 and S2†).

Modelling approach

Flow reactor model

Thermal DRM experiments were modeled and simulated with the DETCHEM software package.[11,55,56] To simulate the experiments, a one-dimensional (in flow direction) plug flow reactor model based on a continuum model approach was used. Assuming steady-state and non-dispersive flow conditions, the model solves mass, species, and pressure drop equations in one dimension. Eqn (4) represents the continuity equation.

$$\frac{\mathrm{d}\rho u}{\mathrm{d}z} = \frac{2}{r}\sum_{i\in S_g} M_i R_i^{\mathrm{surf}}, \tag{4}$$

where u is the gas velocity, ρ is the gas-phase density, z is the axial coordinate of the cylindrical reactor, r is the radius of the empty-tube reactor, S_g is the set of gas-phase species, M_i is the molar mass of the species i, R_i^{surf} is the effective molar production rate of the gas-phase species i by surface deposition reactions. The mass balance for species based on gas-phase and surface deposition reactions is given in eqn (5).

$$\rho u\frac{\mathrm{d}Y_i}{\mathrm{d}z} + \frac{2}{r}Y_i\sum_{i\in S_g} M_i R_i^{\mathrm{surf}} = M_i\left(\frac{2}{r}R_i^{\mathrm{surf}} + R_i^{\mathrm{gas}}\right), \tag{5}$$

where Y_i is the mass fraction of gas-phase species i, R_i^{gas} is the effective molar production rate of gas-phase species i by gas-phase reactions. Furthermore, the present model computes the residence time based on the eqn (6) shown below.

$$\frac{\mathrm{d}\tau}{\mathrm{d}z} = \frac{1}{u}, \tag{6}$$

where τ is the residence time. Finally, the model calculates the pressure drop in a cylindrical reactor, as shown in eqn (7).

$$\frac{\mathrm{d}p}{\mathrm{d}z} = -f\frac{\rho u^2}{4r}, \tag{7}$$

where p is the pressure and f = (64/Re) is the friction factor calculated based on the Reynolds number Re (Re < 2300). The simulations presented in our present work focus on spatially resolved species profiles, reaction rates, and surface coverages, omitting the energy balance to avoid additional complexity and computational load. Discrepancies often arise in temperature predictions from models due to uncertainties in heat transfer and potential temperature gradients. Therefore, the experimentally determined temperature profile in the reactor is implemented as user-defined function.

In this study, the deposition reaction is examined as a function of time. For this, transient simulations were conducted using the computer code $\mathrm{DETCHEM}^{\mathrm{PFR\_transient}}$, which acts as a transient wrapper for the one-dimensional plug flow reactor model ($\mathrm{DETCHEM}^{\mathrm{PFR}}$). The $\mathrm{DETCHEM}^{\mathrm{PFR\_transient}}$ simulation assumes that the time scale for deposition reactions substantially exceeds the residence time that is sufficient for gas-phase reactions. In this model, the transient wrapper operates the $\mathrm{DETCHEM}^{\mathrm{PFR}}$ simulation in an iterative manner for each time step. In each step, it performs a near-steady-state analysis to determine the changing concentrations of gas-phase species, while keeping the concentrations of deposition species constant. The coverage of these species can differ based on their position within the reactor. After calculating these local concentrations in the gas-phase, this information is fed back into the transient wrapper, which then updates the concentrations according to eqn (8) through a time-integration step. To finalize the simulation, the process involves a repeated steady-state plug flow simulation, but with revised inlet conditions and an updated surface state.

$$\frac{\mathrm{d}c_i^{\mathrm{surf}}}{\mathrm{d}t} = R_i^{\mathrm{surf}}\left(c_i^{\mathrm{gas}},\ c_i^{\mathrm{surf}}\right), \tag{8}$$

Herein, c_i^{gas} is the concentration of gas-phase species i, and c_i^{surf} is the concentration of the deposition species i.

Reaction mechanisms

Detailed gas-phase kinetic mechanisms by Appel *et al.*[57] (hereinafter referred to as ABF2000), Blanquart *et al.*[58] (Caltechmech), and Porras *et al.*[59] (Polymech) were reviewed in the current work. Moreover, the present study focuses on a temperature range between 1273 to 1673 K, where solid carbon formation can take place as well.[10,48] Therefore, a

carbon deposition mechanism[60] was coupled to the above-mentioned gas-phase mechanisms.

ABF2000 was developed for describing the combustion and pyrolysis of light hydrocarbons. The mechanism consists of oxidation and pyrolysis reactions of C_1 and C_2 species and comprises also carbon coupling reactions as well as the formation of polycyclic aromatic hydrocarbons (PAHs) up to pyrene ($C_{16}H_{10}$). Additionally, the oxidation of aromatic species is incorporated. The mechanism consists of 99 species and 538 reactions.

Caltechmech was developed for describing the combustion of small as well as large hydrocarbons along with the prediction of soot precursors. It starts from reactions of smaller hydrocarbons such as CH_4, C_2H_2, ethylene (C_2H_4), and ethane (C_2H_6), as well as intermediate hydrocarbons such as propadiene (C_3H_4), propylene (C_3H_6), and propane (C_3H_8). It also considers larger hydrocarbons such as *n*-heptane, iso-octane, benzene, and toluene. Furthermore, the mechanism considers the formation of PAHs until cyclopenta(cd)pyrene ($C_{18}H_{10}$). The comprehensive mechanism consists of 149 species and 1651 reactions.

Polymech was developed in order to describe dimethyl-ether and CH_4 combustion. The oxidation and pyrolysis of C_1–C_4 species exists as a sub-mechanism along with a dimethyl-ether sub-mechanism. The mechanism consists of 83 reactions and 558 reactions and comprises an extensive set of reactions for smaller hydrocarbons up to C_6.

Although all three gas-phase mechanisms discussed above are in principle suitable for describing processes taking place under the operating conditions considered in our present work, a brief comparison of the three mechanisms (*cf.* Fig. S1†) uncovers some differences. ABF2000 consists of reactions from light hydrocarbons to PAHs and is computationally the fastest among the three mechanisms considered herein. However, it lacks certain C_3 species intermediates such as C_3H_6, which can play a role according to Polymech. In turn, Polymech considers these intermediates and their corresponding reaction steps, however, species larger than benzene (C_6H_6) are missing. Finally, Caltechmech is the most comprehensive mechanism among the three and is therefore considered for coupling with deposition reactions.

Apart from the gas-phase mechanisms, also a deposition mechanism was considered in this work. The by-products formed in the gas-phase mechanisms were coupled to deposition reactions in order to describe the formation of solid carbon. It consists of 6 species, namely CH_4, C_2H_6, C_2H_4, C_2H_2, C_4H_6, and C_6H_6. After coupling, gas-phase and deposition reactions take place in parallel as illustrated in Fig. 2. Solid carbon deposits on the reactor wall while H_2 is simultaneously released from the gas-phase precursors.[61] Furthermore, H_2 acts as an inhibitor to deposition reactions due to the formation of stable hydrogen–carbon surface complexes.[62] Therefore, inhibition functions were also considered for each deposition reaction. More details about the deposition reactions and their coupling with gas-phase reactions is available in our previous publication.[60] All the mechanisms and kinetic parameters used herein are provided in the supplementary information (Table S3†).

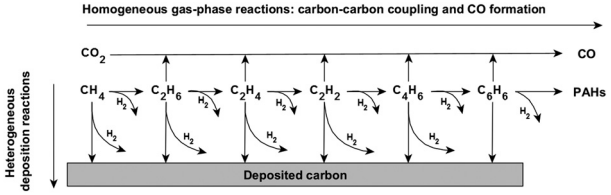

Fig. 2 Schematic of gas-phase reactions and carbon deposition reactions.

Results and discussion

Thermodynamic analysis

Various hydrocarbon gas-phase species along with H_2, CO, and solid carbon can be formed during thermal dry reforming. Using DETCHEM^{EQUIL} from the DETCHEM software package,[55,56] the equilibrium product distribution was calculated for feed mixtures with a $CH_4:CO_2$ ratio of either 1 or 4 under isothermal and isobaric conditions. Fig. 3 displays the respective equilibrium product distribution of major species, considering gas-phase species from Caltechmech and additional graphitic carbon species.

At 1 bar, the CH_4 from the feed remains mostly unconverted only at lower temperatures, whereas it is entirely consumed at temperatures above 873 K. The formation of the gaseous products H_2 and CO is energetically favored at higher temperatures. Notably, the thermodynamic stability of graphitic carbon depends significantly on the $CH_4:CO_2$ ratio. For a $CH_4:CO_2$ ratio of 4, the formation of solid graphitic carbon is thermodynamically possible throughout the entire temperature range investigated in this study. In contrast, for a $CH_4:CO_2$ ratio of 1, the formation of graphitic carbon is favored only at

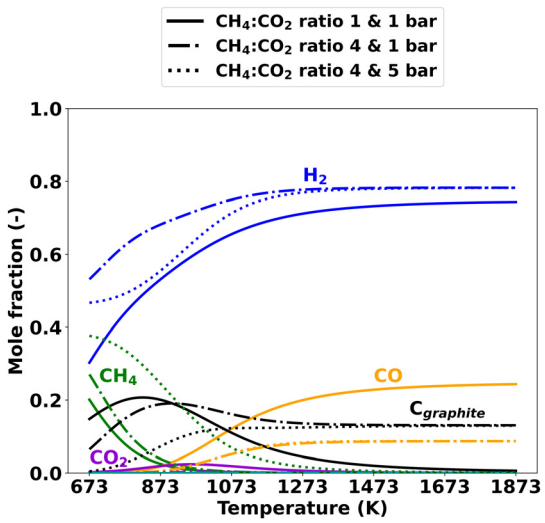

Fig. 3 Effect of different $CH_4:CO_2$ ratios and pressure on the equilibrium product distribution.

temperatures below 1673 K. A pressure increase from 1 bar to 5 bar impacts the product composition particularly at temperatures between 673 K and 1373 K: the pressure increase suppresses CH_4 conversion and thus the formation of graphitic carbon as well as H_2 formation.

In contrast, the influence of pressure on the CO mole fractions is negligible. In fact, due to its exothermic nature, the Boudouard reaction, as depicted in eqn (9), is known to result in graphitic carbon deposition primarily at temperatures below 1273 K.[51,63]

$$2CO \rightleftharpoons C + CO_2 \quad \Delta_R H^\circ = -172 \text{ kJ mol}^{-1} \tag{9}$$

An increase in pressure is associated with a rise in carbon deposition through the Boudouard reaction.[63] However, CH_4 pyrolysis (eqn (1)) can result in carbon deposition above 800 K; while higher temperatures promote carbon formation, an increase in pressure suppresses pyrolytic deposition reactions.[63–65] Therefore, under the conditions employed in the present study that focuses on comparably high temperatures of 1273 K and above, CH_4 pyrolysis emerges as the dominant pathway for carbon deposition. Furthermore, note that C_2 hydrocarbon by-products such as C_2H_2, C_2H_4, and C_2H_6 are formed in negligible quantities (*cf.* Fig. S2†) and other hydrocarbons such as C_3H_6 and C_6H_6 are essentially irrelevant.

In summary, the thermodynamic analysis reveals that elevated temperatures benefit thermal DRM. Furthermore, a $CH_4:CO_2$ ratio above 1 can result in the formation of solid carbon across the entire range of temperatures subject to this study and the $CH_4:CO_2$ ratio also significantly influences the H_2/CO ratio in the resulting syngas. The influence of pressure is of particular relevance below 1373 K, as thermodynamics indicate that intermediate to low temperatures and high pressure are disadvantageous for the DRM reaction.

Comparison of experiments with simulations

Impact of temperature. This section discusses the impact of temperature on thermal dry reforming. For this, simulations were performed with coupled gas-phase and deposition kinetics, considering the actual axially resolved temperature profiles that were measured along the reactor length. End-of-pipe data obtained during experiments with a constant $CH_4:CO_2$ ratio of 2, τ of 5 s, and 1 bar pressure are used for validation.

Fig. 4 illustrates the end-of-pipe mole fractions for both experiments and simulations. Note that the experimental data are presented with error bars set to 5% in order to account for uncertainties in gas species quantification by mass spectrometry.[48] The fraction of the feed gas component CH_4 steadily decreases with temperature and reaches negligible levels above 1673 K at the reactor outlet. In the temperature range of 1273 K to 1373 K, CO forms rapidly as CO_2 is consumed. However, CO formation increases steadily above 1473 K even when CO_2 is fully depleted. H_2 shows a unique trend in both experiments and simulations: first it is

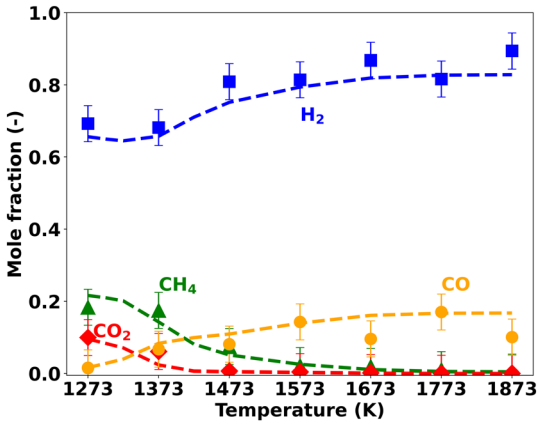

Fig. 4 End-of-pipe experiments *vs.* simulations at different hot zone temperatures at constant $CH_4:CO_2$ ratio = 2, τ = 5 s, and p = 1 bar.

consumed up to 1373 K, but then hydrogen forms in increasing quantity above 1423 K. Other hydrocarbon by-products such as C_2H_2, C_2H_4, C_2H_6, and C_6H_6 are formed in very small quantities and remain below 1% for all the temperatures considered herein (*cf.* Fig. S3†). Given the very small quantities, which are near the detection limit of the analytics, the model matches the experimental end-of-pipe measurement data fairly well.

Since the lab reactor used for the present study consists of a pre-heating zone, an isothermal hot zone, and a post-cooling zone that results in a non-isothermal temperature profile that can have a significant impact on the process (*cf.* Fig. 1), an accurate analysis of the system requires species concentration data with axial resolution.

Fig. 5 illustrates such axial temperature profiles along with the main species mole fractions at hot zone temperatures of 1373 K (Fig. 5(a)) and 1673 K (Fig. 5(b)) as predicted by means of simulations. At 1373 K (Fig. 5(a)), CH_4 and CO_2 consumption start at the beginning of the hot zone. As the reaction progresses along the reactor length, CO and H_2O are formed at a nearly equal rate, yielding almost identical molar fractions. H_2 is consumed as well, however, its consumption rate is lower compared to CH_4 and CO_2. When the temperature is increased to 1673 K while keeping all other parameters unchanged (Fig. 5(b)), the trends change considerably. Once the temperature in the heating zone exceeds approx. 1300 K (corresponding to a reactor length of ~0.26 m), CH_4 and CO_2 consumption sets in, which is well before the reaction gas mixture reaches the actual isothermal hot zone that starts at 0.35 m. Notably, CO_2 is fully depleted already before the hot zone starts. Furthermore, H_2 exhibits a minimum in front of the hot zone, but rapidly increases afterwards, resulting in net H_2 production at the reactor outlet. H_2O formation is observed upon the onset of feed gas species conversion. In contrast to the overall increasing water levels along the reactor length observed at 1373 K, the H_2O concentration peaks after approx. 0.33 m if the hot zone temperature is set to 1673 K; subsequently, the molar fraction of H_2O depletes again and reaches almost zero at the

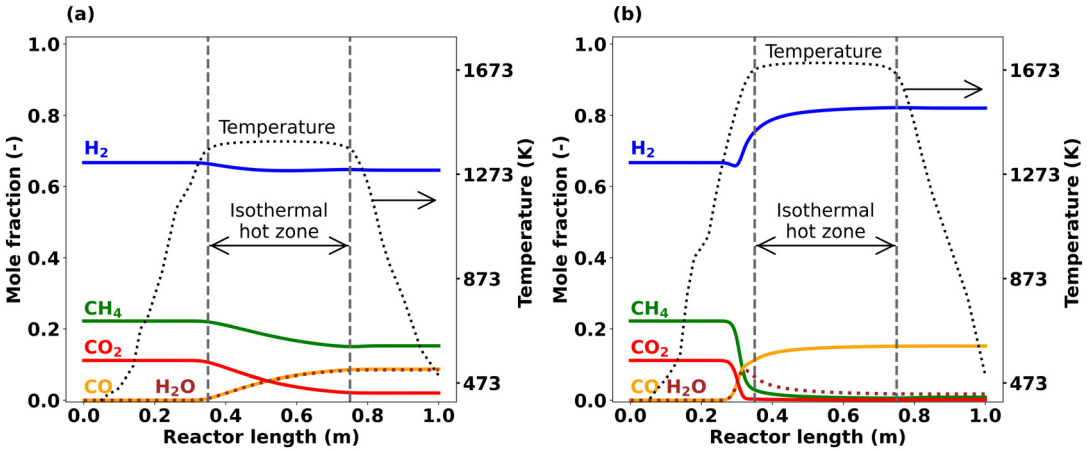

Fig. 5 Simulated axial profiles of main species at CH_4 : CO_2 ratio = 2, τ = 5 s, and p = 1 bar; (a) T = 1373 K, (b) T = 1673 K.

reactor outlet. CO formation is most pronounced right in front of the isothermal hot zone and its level continues to increase only marginally towards the end of the hot zone.

In addition to these main products, hydrocarbon by-products as well as carbon deposition play a major role at 1673 K, as underscored by the axial profiles depicted in Fig. 6. According to the simulation data plotted in Fig. 6(a), C_2H_2 is the most important hydrocarbon formed at 1673 K, whose mole fraction reaches a sharp maximum of about 0.036 just before the start of the hot zone (at about 0.33 m). The C_2H_4 and C_6H_6 mole fractions exhibit maxima around the same axial position, however at significantly lower levels (less than 0.005). None of these hydrocarbons survives until the reactor outlet, since they are consumed during carbon formation and deposition reactions that take place particularly on the reactor wall. Fig. 6(b) shows the deposited carbon amount along the reactor length after 1800 s of reactor operation. The data suggest that carbon deposition is most pronounced right in front of the hot zone, which is the same position where the hydrocarbon concentrations peak according to the data plotted in Fig. 6(a). To understand the different trends at different temperatures, a detailed analysis of the reaction system is mandatory. Therefore, an integral reaction flow analysis (RFA)[64,66] was performed for the Caltechmech gas-phase mechanism, which reveals the consumption and formation of each species.

Fig. 7 shows the results for an RFA conducted for a temperature of 1373 K, a residence time τ of 5 s, and a CH_4 : CO_2 ratio of 2. According to the RFA, all the feed species, namely CO_2, CH_4, and H_2, are consumed under these operating conditions. CO_2 is reduced by an H radical originating either from H_2 or CH_4 decomposition, which results in the formation of CO and the release of an OH radical; this OH radical attacks the H_2 molecule, which yields H_2O as main product. Moreover, the OH radical plays an important role in CH_4 dissociation into a CH_3 (and an H) radical, which is crucial for the following sequential C–C coupling reactions. The first step of C–C coupling reactions is the combination of two CH_3 radicals to form C_2 species, namely C_2H_6, which dehydrogenates to C_2H_4. In the next step, the CH_3 radical attacks C_2H_4 and results in C_3 species formation. However, since the reaction barely progresses

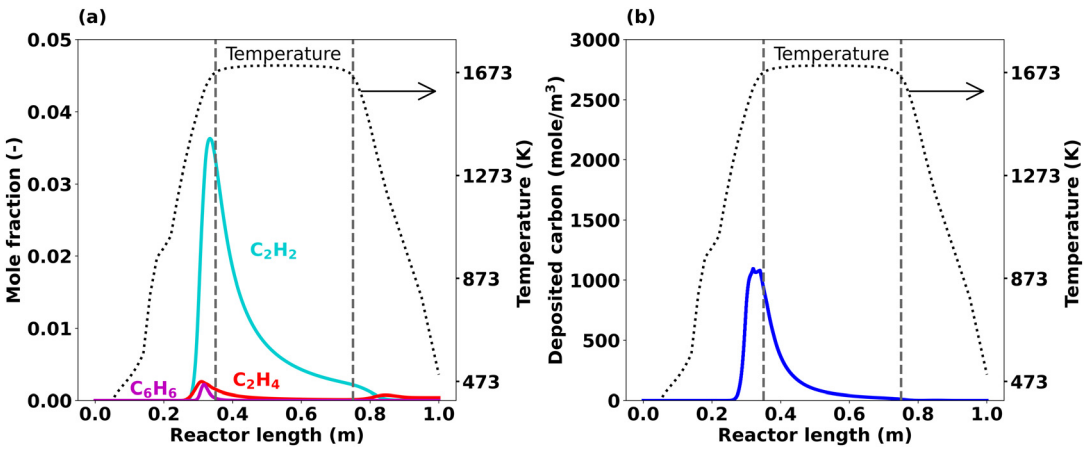

Fig. 6 Simulated axial profiles at 1673 K, CH_4 : CO_2 ratio = 2, τ = 5 s and p = 1 bar; (a) hydrocarbon by-products, (b) deposited moles of carbon along the reactor axis after 1800 s of reactor operation.

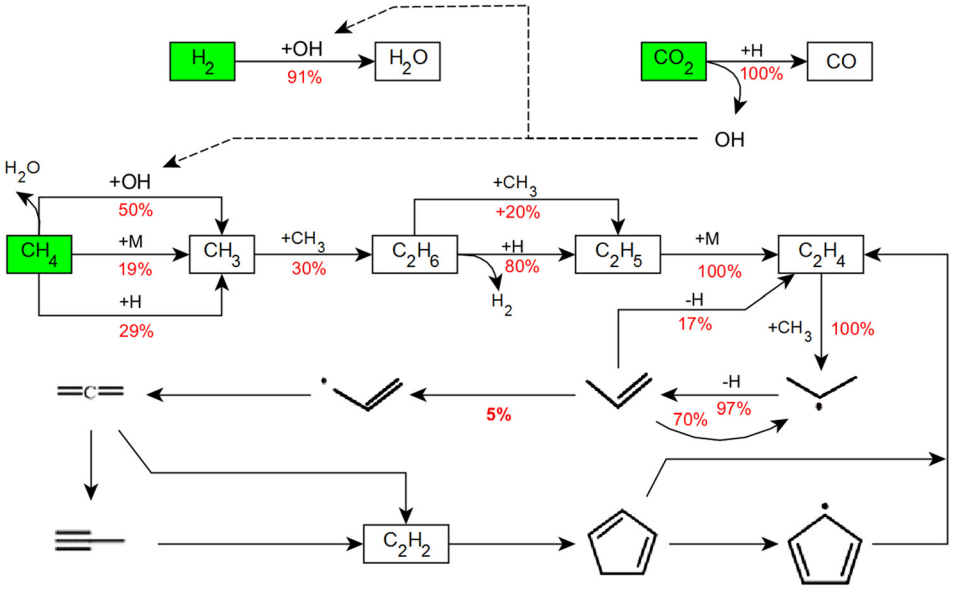

Fig. 7 Integral reaction flow analysis at 1373 K for τ = 5 s, $CH_4:CO_2$ ratio = 2, and p = 1 bar.

further than C_3H_6, C_3 species formation is a rather dead end of the reaction sequence – only 5% of the C_3H_6 molecules react to allyl radicals (C_3H_5) – and H_2O and CO represent the main products at 1373 K. Propylene (C_3H_6) formation has been reported previously to take place during the CH_4 pyrolysis reaction sequence if instead of H_2 argon was used to dilute the feed.[65] In the current work, RWGS, which consumes H_2, creates similar process conditions, which enable the formation of C_3H_6 intermediates. The progression of the reaction beyond C_3H_6 to C_2H_2 and aromatic rings is kinetically limited at 1373 K. C_2H_2 and C_5 rings that are formed in negligible quantities beyond C_3H_5 do not remain stable and are completely opened back to C_2H_4.

In contrast, the RFA that was performed at 1673 K while keeping both the residence time τ (5 s) and the $CH_4:CO_2$ ratio (2) constant suggests that the reaction pathways become substantially more complex if the temperature is increased by 300 K (Fig. 8). At this temperature, CH_4 and CO_2 are consumed while there is a net rate of production for H_2. CO_2 is fully converted to CO under release of an OH radical. Note that compared to 1373 K, the role of the OH radical in the activation of CH_4 is much less pronounced at 1673 K. Furthermore, CH_4 dissociation into CH_3 and H radicals primarily takes place *via* an H radical attack at 1673 K. The reaction steps that lead to C_2H_2 formation *via* a C–C coupling reaction are similar to those at lower temperature. However, the reaction progression from C_3H_6 onwards is more than doubled (5% at 1373 K *versus* 11% at 1673 K). Although the formation of the first aromatic ring (mostly benzene) takes place *via* C_3 intermediates, C_2H_2 is the central species according to the RFA: C_3 intermediates are partially cracked to C_2H_2 and most of the aromatic rings also produce C_2H_2 when opened. Furthermore, the RFA suggests that OH radicals react with C_2H_2 molecules to significant extent, which enables the formation of CO from hydrocarbons. From C_6H_6 onwards, the addition of a CH_3 radical leads to toluene (C_7H_8) formation. In the following steps, PAHs are formed *via* the addition of C_3H_3 or benzyl radicals. Although OH radicals also attack aromatic molecules such as C_6H_6 and naphthalene to form phenol and 2-naphthol, respectively, these molecules are unstable and quickly form hydrocarbon products, hereby releasing CO.

Overall, the temperature is a parameter that greatly influences both the DRM reaction progression as well as the product distribution. At lower temperatures up to 1373 K, H_2 is consumed as underscored by the data plotted in Fig. 4 and 5(a). As revealed by the RFA results (Fig. 7), H_2 is consumed during H_2O formation *via* the RWGS reaction (eqn (3)) while at the same time CO_2 is converted into CO. On the other hand, the progress of C–C coupling reactions that release H_2 are limited. C_2H_2, which is the key species with regard to carbon deposition reactions,[10,58,60,64] is also formed only in negligible quantity. Therefore, there is a net consumption of H_2 at 1373 K. In contrast, at 1673 K there is a net production of H_2 as depicted in Fig. 4. However, the axial profile simulated for a reaction temperature of 1673 K (Fig. 5(b)) suggests different reaction regimes along the reactor length. It uncovers that H_2 is consumed in the pre-heating zone at temperatures between 1273 K and 1423 K, and then rises rapidly. Between 1273 K and 1423 K, the RWGS reaction (eqn (3)) is dominant and results in H_2O and CO production. As underscored by the RFA results plotted in Fig. 8, a temperature increase to 1673 K facilitates C–C coupling reactions. The coupling reactions and subsequent gas-phase dehydrogenation reactions generate all the species involved in the carbon deposition mechanism. The surface deposition reactions further release the H_2 in the gas-phase while forming the solid carbon layer on the reactor wall. Therefore, net H_2 formation is observed at 1673 K. After all, RWGS is the dominating reaction in the

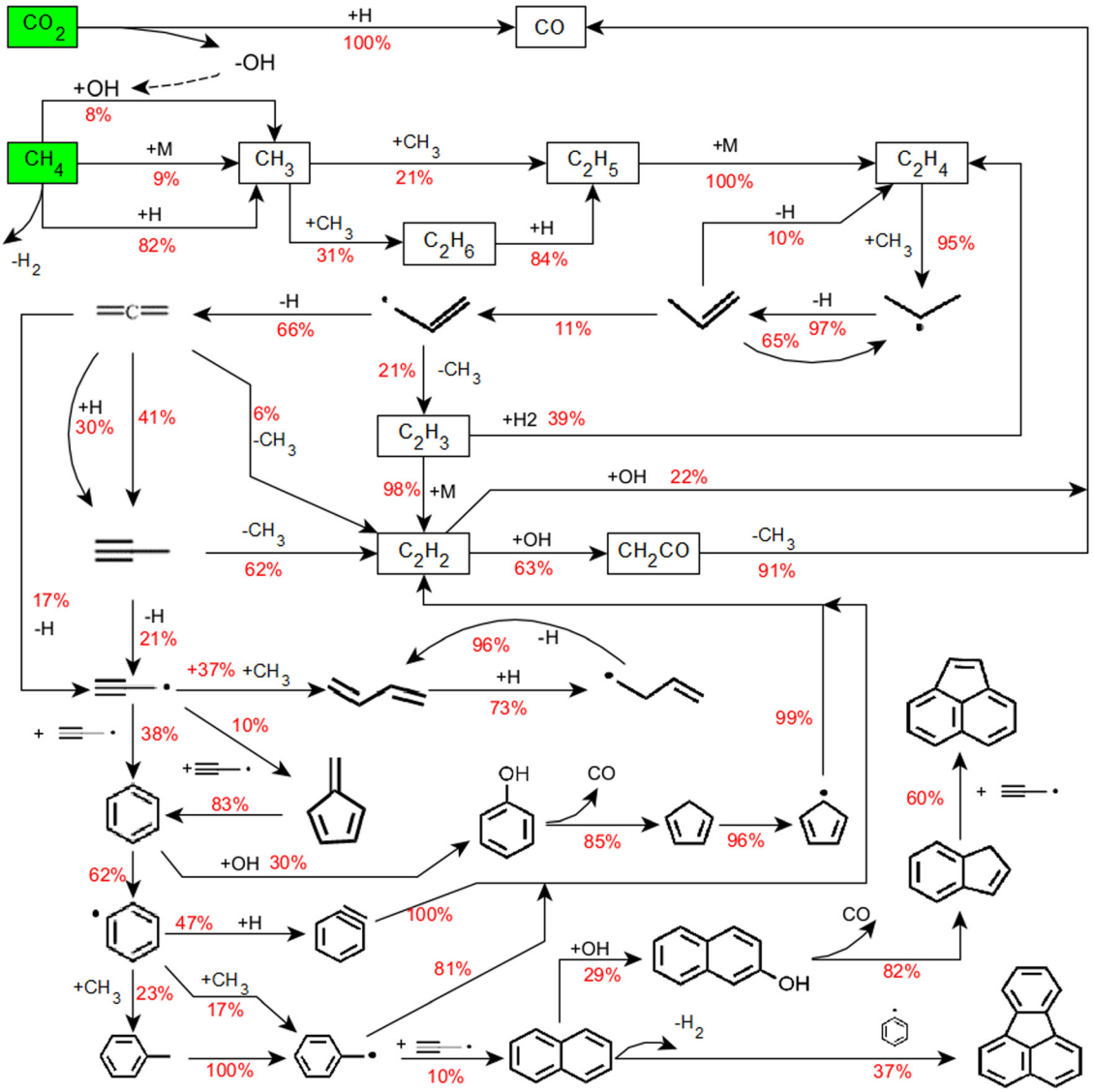

Fig. 8 Integral reaction flow analysis at 1673 K for τ = 5 s, $CH_4:CO_2$ ratio = 2, and p = 1 bar.

temperature regime between 1273 K and 1423 K, and CH_4 pyrolysis dominates above 1473 K. Consequently, the temperature regime governs the predominant reaction that activates the CH_4 molecule in the gas-phase and thus directly affects C–C coupling reactions and ultimately carbon deposition as well. This becomes particularly clear when the two small peaks in the deposition profiles in Fig. 6(b) are considered. At higher temperature H_2O is split into H and OH radicals. These OH radicals can then attack aromatic hydrocarbons, which are cracked to release CO. Sustained CO formation even after complete depletion of CO_2 is a result of this reaction sequence and explains the continuous rise of the CO mole fraction in Fig. 5(b). At 1673 K, τ = 5 s, and a $CH_4:CO_2$ ratio of 2, 38% of CH_4 from the feed react to CO, whereas 52% of CH_4 are captured in the form of solid carbon that deposits on the reactor walls and at the bottom of the reactor. These findings underscore the major importance of both, gas-phase and deposition reactions. Considering the experimental error bars of 5%, the simulations are in good agreement with the experiments. Notably, beyond a mere description of the end-of-pipe data, the axially resolved species profiles as well as the RFA allow to explain the complex reaction chemistry during thermal DRM.

Impact of CH_4 and CO_2 co-feeding. The impact of CO_2 co-feeding with varying $CH_4:CO_2$ ratios is studied in this section. Fig. 9 illustrates the end-of-pipe mole fractions of both experiments and numerical simulations for different $CH_4:CO_2$ ratios in the feed gas, while keeping temperature (T = 1673 K), residence time (τ = 5 s), and pressure (p = 1 bar) constant. Analogous to the data discussed in the previous section, the experimental data exhibit error bars of 5%. Overall, decreasing the $CH_4:CO_2$ ratio from 4 to 1 leads to increased CO formation and a suppression of H_2 formation. CO_2 is completely consumed in all cases, whereas traces of CH_4 can be seen at the reactor outlet for the $CH_4:CO_2$ ratio of 3 and higher. Hydrocarbon by-products remain below 0.2% under all conditions (*cf.* Fig. S4†).

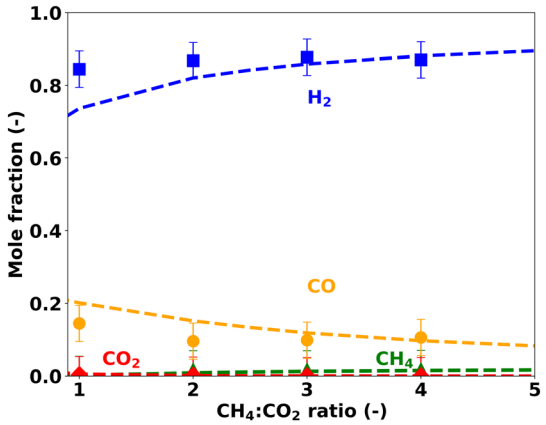

Fig. 9 End-of-pipe experiments *vs.* simulations at different $CH_4:CO_2$ ratios keeping the T = 1673 K, τ = 5 s, and p = 1 bar constant.

Since analyzing axial profiles is essential for a comprehensive understanding of the impact of the $CH_4:CO_2$ ratio, Fig. 10 shows axially resolved mole fraction profiles for the main gas-phase species H_2, CH_4, CO_2, and CO as well as for the deposition of carbon that were simulated for $CH_4:CO_2$ ratios of 1 and 4. For a $CH_4:CO_2$ ratio of 1, H_2 shows a sharp drop prior to the hot zone, which points to a consumption of H_2. Subsequently, the H_2 mole fraction increases along the reactor length and results in a net H_2 production by the reactor outlet (Fig. 10(a)). For a higher $CH_4:CO_2$ ratio of 4, the minimum of H_2 disappears and H_2 steadily increases along the reactor length, resulting in a pronounced net H_2 production at the reactor outlet. Since the feed gas contains more CH_4 if a $CH_4:CO_2$ ratio of 4 is chosen, C–C coupling reactions and thus C_2H_2 formation are promoted (Fig. S5†). Higher C_2H_2 levels ultimately lead to higher carbon deposition, which is supported by the data depicted in Fig. 10(b).

Overall, the $CH_4:CO_2$ ratio is the key process parameter to control the H_2/CO ratio of the effluent syngas. For a $CH_4:CO_2$ ratio of 1 in the feed, the end-of-pipe H_2/CO syngas ratio is 3.6, but it increases to 9 when a $CH_4:CO_2$ ratio of 4 is chosen instead. However, note that the H_2-rich syngas at the reactor outlet is also a result of the H_2 content in the feed gas stream, as the reaction gases are diluted by 66.7% H_2 prior to entering the reactor. Typical processes in chemical industry that rely on syngas, *e.g.* the synthesis of methanol, oxo-alcohols, and the Fischer–Tropsch process, require a H_2/CO ratio of approx. 2.[21] Therefore, integrating syngas production into chemical production would call for an adjustment of the H_2/CO ratio. Notably, most of the worldwide syngas demand is currently covered by production *via* SMR,[15] which commonly results in syngas with an H_2/CO ratio between 2.8 and 4.8.[21,67] Therefore, syngas produced by thermal DRM from feeds with comparably low $CH_4:CO_2$ ratios might be used to replace syngas produced in SMR plants, which enables the direct use of existing downstream infrastructure.

As an alternative, a mixture of only CH_4 and CO_2 without H_2 dilution could be used as feed. Under the assumption of a hypothetical $CH_4:CO_2$ ratio of 1.86, a syngas H_2/CO ratio of 2 can be attained end-of-pipe according to the axially resolved simulation data shown in Fig. 11. However, the higher CH_4 levels in the feed gas go along with a higher carbon formation and deposition on the reactor walls as well as with a relatively high H_2O formation. In general, thermal DRM represents a remarkably versatile reaction system. By considering downstream gas processing units and the constraints of reactor design, it is possible to obtain a wide range of syngas qualities based on a rational choice of the feed gas composition.

Impact of residence time. In addition to temperature and feed gas composition, also the residence time (τ) in the hot zone of the reactor matters during thermal DRM, which is addressed in this section. For this, τ is varied from 1 s to 7 s in the experiments and the data are compared to the simulations (Fig. 12). The data suggest an only limited impact of τ on the molar fractions of H_2, CO, CH_4, and CO_2. The experimentally determined variations observed remain

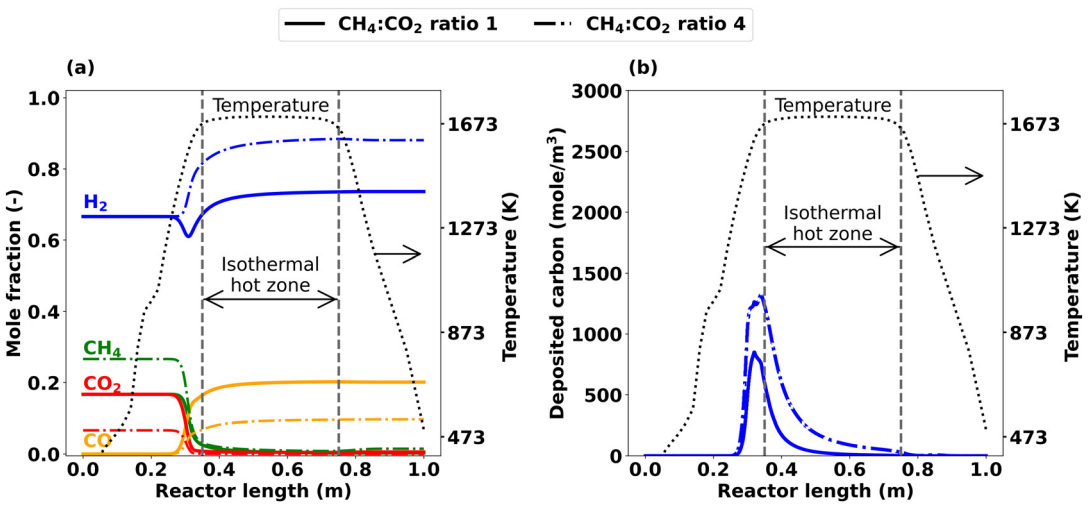

Fig. 10 Simulated axial profiles for $CH_4:CO_2$ ratio 1 and 4 at T = 1673 K, τ = 5 s and p = 1 bar; (a) main species, (b) carbon deposition after 1800 s.

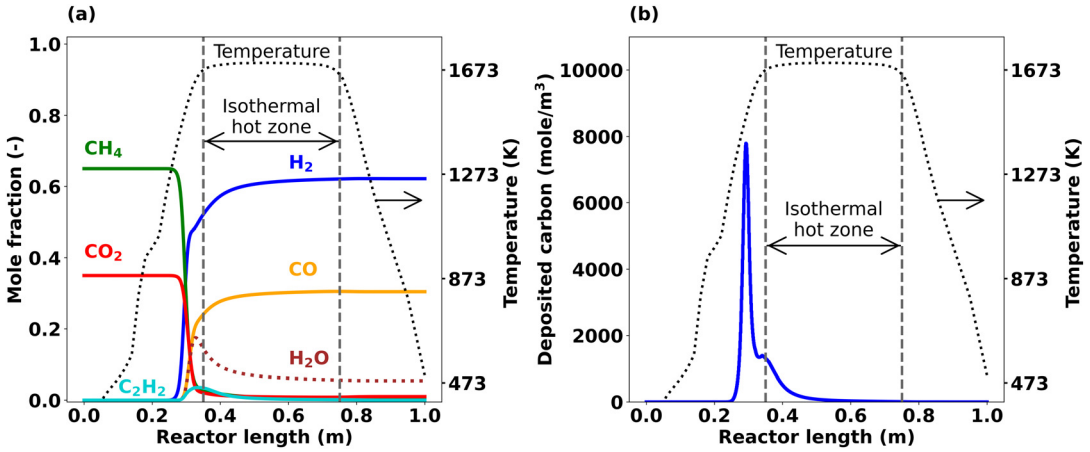

Fig. 11 Simulated axial profiles with CH_4 : CO_2 molar ratio of 1.86, without H_2 in feed and T = 1673 K, τ = 5 s and p = 1 bar; (a) gas-phase species, (b) carbon deposition after 1800 s. From the CH_4-borne carbon, only a minor share remains in the gas-phase as hydrocarbons, while 33% of the CH_4-borne carbon is transformed into CO and 48% of CH_4-borne carbon is captured as solid carbon.

within the limits of the error bars (5%), but the simulations show a slight increase in the H_2 formation at τ of 7 s compared to 1 s. Note that hydrocarbon by-products are below 1% (*cf.* Fig. S6†).

The axially resolved mole fraction profiles illustrated in Fig. 13 enable a more detailed understanding and ultimately offer an explanation for the trends observed. The profiles obtained at a residence time τ of 1 s and 7 s differ most at a reactor length of approx. 0.32 m, as more CH_4 and CO_2 are consumed during the onset of the reaction if a residence time of 7 s is chosen instead of 1 s (Fig. 13(a)). Similarly, H_2 and CO are formed earlier in the reactor for τ = 7 s. These residence time-induced differences become smaller towards the reactor outlet. Although the end-of-pipe gas-phase concentrations deviate only to a minor extent, residence time variations exhibit a significant impact on carbon deposition: as shown by the simulation data in Fig. 13(b), the carbon formation and deposition along the reactor axis is much higher at τ of 1 s compared to 7 s.

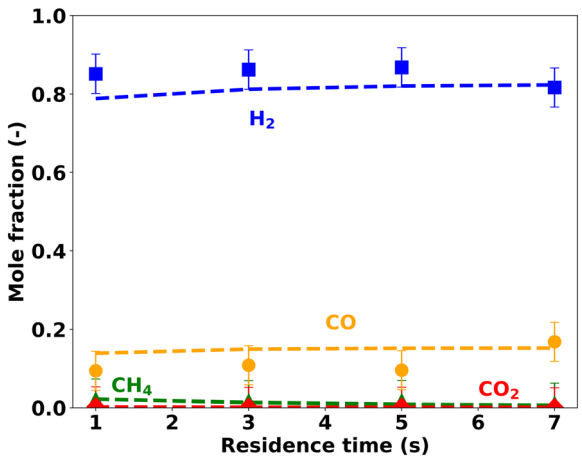

Fig. 12 End-of-pipe experiments *vs.* simulations at different residence times keeping T = 1673 K, CH_4 : CO_2 ratio = 2, and p = 1 bar.

Notably, a lower residence time is achieved by increasing the mass flow rate of the feed gas (*cf.* Table S1†). Consequently, more CH_4 molecules enter the reactor at τ of 1 s compared to 7 s, which results in a substantial increase in deposited carbon from 0.35 g at 7 s to 1.95 g at 1 s. With regard to technical applications, these findings are of high relevance as carbon deposition can cause reactor clogging. However, innovative reactor designs such as the use of a carbon moving bed, *e.g.* as proposed by BASF SE in the context of methane pyrolysis, might be a useful concept for thermal DRM processes as well.[68]

Since carbon formation is a consequence of C–C-coupling and dehydrogenation reactions, also the by-products, C_2 species in particular, are strongly influenced by variations of the residence time τ, which is illustrated in Fig. 14. At τ = 7 s, the share of C_2 species by the end of the reactor is 0.04%, which rises to 1.4% when τ is reduced to 1 s. Previous studies have focused on the pyrolysis of natural gas at short residence times, typically below 1 s, and especially investigated C_2 species formation.[18,69,70] Our present results indicate that τ is a crucial process parameter regarding carbon deposition also in the 1 s to 7 s range. However, the primary products at these conditions are H_2 and CO, whereas at smaller residence times the C_2 fraction in the products increase. Moreover, the fraction of CH_4 converted into CO and solid carbon also changes considerably with τ. At 1 s, 27% CH_4 are converted into CO, 42% into captured deposited carbon, and 32% remain in the gas-phase in the form of other hydrocarbons. Increasing τ to 7 s enables to capture 53% of the CH_4 in the form of elemental carbon that deposits in the reactor, while 38% are converted into CO, and only 8% remain in the gas-phase in the form of other hydrocarbons.

Conclusions

In the present study, thermal dry reforming of methane was studied for a wide range of operating conditions by combining

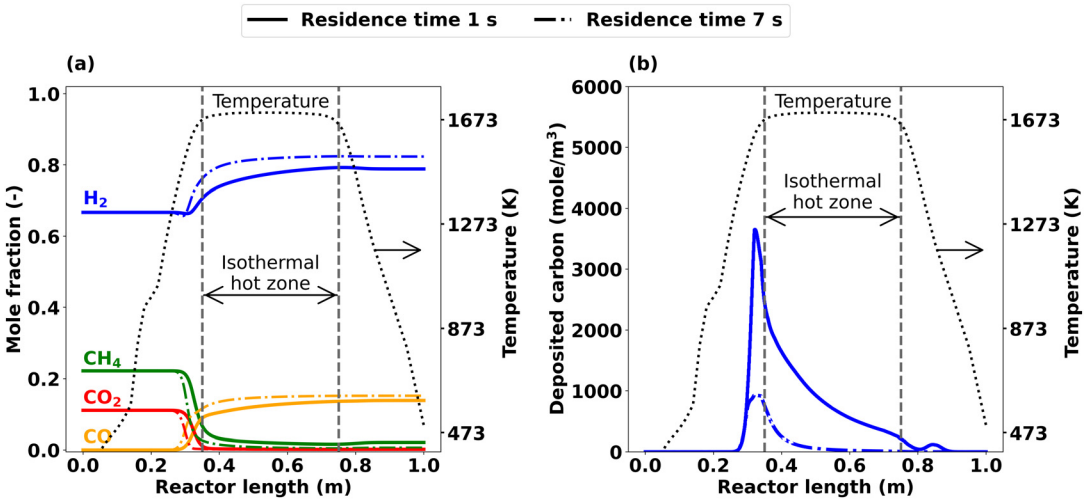

Fig. 13 Simulated axial profiles for τ of 1 s and 7 s at $CH_4:CO_2$ ratio = 2, T = 1673 K and p = 1 bar; (a) main species, (b) carbon deposition after 1800 s.

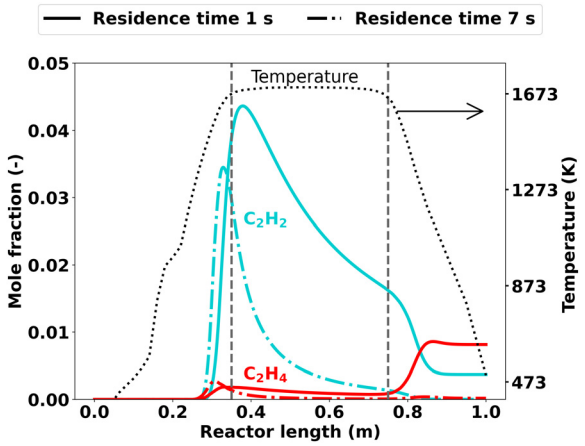

Fig. 14 Simulated axial profiles of C_2H_2 and C_2H_4 for τ of 1 s and 7 s at $CH_4:CO_2$ ratio = 2, T = 1673 K and p = 1 bar.

numerical simulations and experiments. A one-dimensional plug flow reactor model was used to study coupled gas-phase and deposition reaction systems. Simulated gas-phase species were compared to the end-of-pipe measurements for model validation.

The deposition model applied herein offers insights into the distribution of carbon deposits along the length of the reactor. Two different temperature-dependent reaction regimes were identified. For lower temperatures between 1273 K and 1373 K, the reverse water-gas shift reaction plays a key role, resulting in the consumption of H_2 and the formation of CO and H_2O. In contrast, methane pyrolysis is the dominating reaction pathway at 1473 K and above and thus facilitates carbon deposition and H_2 production. For a $CH_4:CO_2$ ratio of 2, a residence time of 5 s, and a pressure of 1 bar, CO_2 was completely consumed when the temperature exceeded 1473 K, mostly forming CO *via* the reverse water-gas shift reaction. In contrast, CH_4 conversion requires higher temperatures. Above 1673 K, CH_4 is fully consumed due to CO formation from dry reforming and carbon deposition from pyrolytic reaction pathways. While under such harsh conditions only small amounts of hydrocarbon species remain in the gas-phase, 38% of the CH_4 from the feed stream are transformed into CO and 52% are captured as solid carbon. The composition of the feed gas, specifically in terms of the $CH_4:CO_2$ ratio and additional H_2 dilution, is a critical parameter for tuning the H_2/CO ratio in the effluent syngas product gas stream. Thus, optimizing the feed gas composition offers great potential to meet specific requirements, such as achieving a particular H_2/CO syngas ratio while simultaneously minimizing or maximizing solid carbon deposition. Although residence time variations between 1 s and 7 s have an only marginal impact on the H_2/CO syngas ratio, reducing the residence time resulted in higher carbon deposition due to higher mass flow rates. In conclusion, all the process parameters varied herein have a relevant influence on the distribution of carbon derived from CH_4, determining the proportion converted into CO and the amount sequestrated as solid deposits on the reactor walls.

Thermal dry reforming of CO_2-containing biogas possesses a great potential to act as a CO_2-negative process while simultaneously producing sustainable syngas as feedstock for valuable chemicals. The combined gas-phase and deposition model used in this study accurately describes the thermal DRM process. Beyond simply serving as a means to validate against experimental data, our model offers an essential advantage by providing detailed axial profiles and quantitative information on deposited carbon, which are challenging to obtain through experimental approaches. Despite the comprehensive chemistry considered in the mechanism used herein, the simulations can be run on a desktop computer within a reasonable time frame. This framework and the insights gained from this work lay a

strong foundation for reactor design and scale-up of the thermal dry reforming process, which may be an industrially viable production route for sustainable syngas.

Data availability

The data supporting this article have been included as part of the ESI.†

Author contributions

Manas Mokashi: writing – original draft, visualization, validation, methodology, investigation, formal analysis, data curation, conceptualization. Akash Bhimrao Shirsath: writing – review & editing, software, formal analysis. Sinan Demir: investigation, formal analysis. Ahmet Çelik: investigation, formal analysis. Patrick Lott: writing – review & editing, supervision, project administration, methodology, data curation, conceptualization. Steffen Tischer: writing – review & editing, supervision, software, formal analysis. Olaf Deutschmann: writing – review & editing, supervision, resources, project administration, funding acquisition, data curation, conceptualization.

Conflicts of interest

There are no conflicts to declare.

Acknowledgements

The authors gratefully acknowledge the omegadot software & consulting GmbH for a cost-free academic license of DETCHEM and H. Müller (ITCP, KIT) for fruitful discussion.

References

1 K. Oshiro and S. Fujimori, *Appl. Energy*, 2022, **313**, 118803.
2 P. Lott and O. Deutschmann, *Proc. Combust. Inst.*, 2023, **39**, 3183–3215.
3 A. González-Garay, M. S. Frei, A. Al-Qahtani, C. Mondelli, G. Guillén-Gosálbez and J. Pérez-Ramírez, *Energy Environ. Sci.*, 2019, **12**, 3425–3436.
4 A. A. Kiss, J. J. Pragt, H. J. Vos, G. Bargeman and M. T. de Groot, *Chem. Eng. J.*, 2016, **284**, 260–269.
5 E. V. Kondratenko, G. Mul, J. Baltrusaitis, G. O. Larrazábal and J. Pérez-Ramírez, *Energy Environ. Sci.*, 2013, **6**, 3112–3135.
6 C. Kim, C. J. Yoo, H. S. Oh, B. K. Min and U. Lee, *J. CO2 Util.*, 2022, **65**, 102239.
7 G. Centi, E. A. Quadrelli and S. Perathoner, *Energy Environ. Sci.*, 2013, **6**, 1711–1731.
8 O. Schmidt, A. Gambhir, I. Staffell, A. Hawkes, J. Nelson and S. Few, *Int. J. Hydrogen Energy*, 2017, **42**, 30470–30492.
9 O. Machhammer, A. Bode and W. Hormuth, *Chem. Ing. Tech.*, 2016, **39**, 1185–1193.
10 P. Lott, M. B. Mokashi, H. Müller, D. J. Heitlinger, S. Lichtenberg, A. B. Shirsath, C. Janzer, S. Tischer, L. Maier and O. Deutschmann, *ChemSusChem*, 2023, **16**, e202300301.
11 A. B. Shirsath, M. Mokashi, P. Lott, H. Müller, R. Pashminehazar, T. Sheppard, S. Tischer, L. Maier, J.-D. Grunwaldt and O. Deutschmann, *J. Phys. Chem. A*, 2023, **127**, 2136–2147.
12 T. Becker, F. Keuchel and D. W. Agar, *Chem. Ing. Tech.*, 2021, **93**, 762–770.
13 N. Sánchez-Bastardo, R. Schlögl and H. Ruland, *Ind. Eng. Chem. Res.*, 2021, **60**, 11855–11881.
14 T. Geißler, A. Abánades, A. Heinzel, K. Mehravaran, G. Müller, R. K. Rathnam, C. Rubbia, D. Salmieri, L. Stoppel, S. Stückrad, A. Weisenburger, H. Wenninger and T. Wetzel, *Chem. Eng. J.*, 2016, **299**, 192–200.
15 G. A. Olah, A. Goeppert and G. K. Surya Prakash, *Methanol Economy*, John Wiley & Sons Ltd, 2009, pp. 143–178.
16 E. Bartholomé, *Chem. Eng. Sci.*, 1954, **3**, 94–104.
17 D. Chen, X. Chen, C. Luo, Z. Liu and L. H. Gan, *Chem. Eng. J.*, 2021, **426**, 130871.
18 B. Baek, B. Nair, I. Lengyel, L. Chen, S. Pannala, R. Vm and D. West, *Ind. Eng. Chem. Res.*, 2021, **60**, 6993–7002.
19 S. Gudiyella, Z. J. Buras, T. C. Chu, I. Lengyel, S. Pannala and W. H. Green, *Ind. Eng. Chem. Res.*, 2018, **57**, 7404–7420.
20 R. Reimert, F. Marschner, H.-J. Renner, W. Boll, E. Supp, M. Brejc, W. Liebner and G. Schaub, *Gas Production, 2. Processes, in Ullmann's Encyclopedia of Industrial Chemistry*, John Wiley & Sons Ltd, 2011, pp. 423–482.
21 E. Schwab, A. Milanov, S. A. Schunk, A. Behrens and N. Schödel, *Chem. Ing. Tech.*, 2015, **87**, 347–353.
22 K. Wittich, M. Krämer, N. Bottke and S. A. Schunk, *ChemCatChem*, 2020, **12**, 2130–2147.
23 J. R. Rostrup-Nielsen, J. Sehested and J. K. Nørskov, *Adv. Catal.*, 2002, **47**, 65–139.
24 M. H. Halabi, M. H. J. M. de Croon, J. van der Schaaf, P. D. Cobden and J. C. Schouten, *Chem. Eng. J.*, 2008, **137**, 568–578.
25 R. Schwiedernoch, S. Tischer, C. Correa and O. Deutschmann, *Chem. Eng. Sci.*, 2003, **58**, 633–642.
26 O. Deutschmann and L. D. Schmidt, *AIChE J.*, 1998, **44**, 2465–2477.
27 S. Hanf, S. Angeli, D. Dussol, C. Fritsch, L. Maier, M. Müller, O. Deutschmann and S. A. Schunk, Chapter 9: Methane Dry Reforming, in: *Chemical Valorisation of Carbon Dioxide*, ed. G. Stefanidis and A. Stankiewicz, The Royal Society of Chemistry, 2022, pp. 187–207.
28 A. Giehr, L. Maier, S. Angeli, S. A. Schunk and O. Deutschmann, *Ind. Eng. Chem. Res.*, 2020, **59**, 18790–18797.
29 L. A. Schulz, L. C. S. Kahle, K. H. Delgado, S. A. Schunk, A. Jentys, O. Deutschmann and J. A. Lercher, *Appl. Catal., A*, 2015, **504**, 599–607.
30 A. Calbry-Muzyka, H. Madi, F. Rüsch-Pfund, M. Gandiglio and S. Biollaz, *Renewable Energy*, 2022, **181**, 1000–1007.
31 D. Zambrano, J. Soler, J. Herguido and M. Menéndez, *Top. Catal.*, 2019, **62**, 456–466.
32 N. Gokon, Y. Yamawaki, D. Nakazawa and T. Kodama, *Int. J. Hydrogen Energy*, 2011, **36**, 203–215.
33 N. E. McGuire, N. P. Sullivan, O. Deutschmann, H. Zhu and R. J. Lee, *Appl. Catal., A*, 2011, **394**, 257–265.

34 M. Maestri, D. G. Vlachos, A. Beretta, G. Groppi and E. Tronconi, *J. Catal.*, 2008, **259**, 211–222.
35 B. Steinhauser, M. R. Reddy, J. Radnik and A. Martin, *Appl. Catal., A*, 2009, **366**, 333–341.
36 Y. Kathiraser, U. Oemar, E. T. Saw, Z. Li and S. Kawi, *Chem. Eng. J.*, 2015, **278**, 62–78.
37 T. Roussière, L. Schulz, K. M. Schelkle, G. Wasserschaff, A. Milanov, E. Schwab, O. Deutschmann, A. Jentys, J. Lercher and S. A. Schunk, *ChemCatChem*, 2014, **6**, 1447–1452.
38 C. Fritsch, J. Titus, T. Roussière, C. Lizandara-Pueyo, R. Müller, R. Gläser and S. A. Schunk, *Chem. Ing. Tech.*, 2022, **94**, 1727–1738.
39 Y. Lin, C. Yang, W. Zhang, H. Machida and K. Norinaga, *Chem. Eng. Sci.*, 2023, **268**, 118380.
40 S. Chen, J. Zaffran and B. Yang, *Appl. Catal., B*, 2020, **270**, 118859.
41 M. Usman, W. M. A. W. Daud and H. F. Abbas, *Renewable Sustainable Energy Rev.*, 2015, **45**, 710–744.
42 C. Pizzolitto, E. Pupulin, F. Menegazzo, E. Ghendini, A. D. Michele, M. Mattarelli, G. Cruciani and M. Signoretto, *Int. J. Hydrogen Energy*, 2019, **44**, 28065–28076.
43 J. O. Ighalo and P. B. Amama, *J. CO2 Util.*, 2024, **81**, 102734.
44 B. Stolze, J. Titus, S. A. Schunk, A. Milanov, E. Schwab and R. Gläser, *Front. Chem. Sci. Eng.*, 2016, **10**, 281–293.
45 J. H. Bitter, K. Seshan and J. A. Lercher, *J. Catal.*, 1999, **183**, 336–343.
46 C. Fukuhara, Y. Matsui, M. Tanebayashi and R. Watanabe, *Chem. Eng. J. Adv.*, 2021, **5**, 100057.
47 L. C. S. Kahle, T. Roussière, L. Maier, K. Herrera Delgado, G. Wasserschaff, S. A. Schunk and O. Deutschmann, *Ind. Eng. Chem. Res.*, 2013, **52**, 11920–11930.
48 A. Çelik, I. Ben Othman, H. Müller, P. Lott and O. Deutschmann, *React. Chem. Eng.*, 2023, **9**, 108–118.
49 D. Chen and L. H. Gan, *Chem. Eng. J.*, 2022, **439**, 135732.
50 V. I. Savchenko, Y. S. Zimin, A. V. Nikitin, I. V. Sedov and V. S. Arutyunov, *J. CO2 Util.*, 2021, **47**, 101490.
51 S. D. Angeli, S. Gossler, S. Lichtenberg, G. Kass, A. K. Agrawal, M. Valerius, K. P. Kinzel and O. Deutschmann, *Angew. Chem., Int. Ed.*, 2021, **60**, 11852–11857.
52 O. V. Shapovalova, Y. N. Chun, M. S. Lim, V. M. Shmelev and V. S. Arutyunov, *Int. J. Hydrogen Energy*, 2012, **37**, 14040–14046.
53 P. Blanck, G. Kass, K. P. Kinzel and O. Deutschmann, *Energy Adv.*, 2024, **3**, 123–130.
54 F. Bustamante, R. M. Enick, A. V. Cugini, R. P. Killmeyer, B. H. Howard, K. S. Rothenberger, M. V. Ciocco, B. D. Morreale, S. Chattopadhyay and S. Shi, *AIChE J.*, 2004, **50**, 1028–1041.
55 A. B. Shirsath, M. L. Schulte, B. Kreitz, S. Tischer, J.-D. Grunwaldt and O. Deutschmann, *Chem. Eng. J.*, 2023, **469**, 143847.
56 O. Deutschmann, S. Tischer, S. Kleditzsch, V. Janardhanan, C. Correa, D. Chatterjee, N. Mladenov, H. D. Minh, H. Karadeniz, M. Hettel, V. Menon, A. Banerjee, H. Gossler, A. Shirsath and E. Daymo, *DETCHEM*, 2022, **https://www.detchem.com**.
57 J. Appel, H. Bockhorn and M. Frenklach, *Combust. Flame*, 2000, **121**, 122–136.
58 G. Blanquart, P. Pepiot-Desjardins and H. Pitsch, *Combust. Flame*, 2009, **156**, 588–607.
59 S. Porras, D. Kaczmarek, J. Herzler, S. Drost, M. Werler, T. Kasper, M. Fikri, R. Schießl, B. Atakan, C. Schulz and U. Maas, *Combust. Flame*, 2020, **212**, 107–122.
60 M. Mokashi, A. B. Shirsath, A. Çelik, P. Lott, H. Müller, S. Tischer, L. Maier, J. Bode, D. Schlereth, S. Frederik, D. Flick, M. Bender, K. Ehrhardt and O. Deutschmann, *Chem. Eng. J.*, 2024, **485**, 149684.
61 K. J. Hüttinger, *Chem. Vap. Deposition*, 1998, **4**, 151–158.
62 A. Becker, Z. Hu and K. J. Hüttinger, *Fuel*, 2000, **79**, 1573–1580.
63 A. Shamsi and C. D. Johnson, *Catal. Today*, 2003, **84**, 17–25.
64 M. Mokashi, A. B. Shirsath, P. Lott, H. Müller, S. Tischer, L. Maier and O. Deutschmann, *Chem. Eng. J.*, 2024, **479**, 147556.
65 A. Çelik, A. B. Shirsath, F. Syla, H. Müller, P. Lott and O. Deutschmann, *J. Anal. Appl. Pyrolysis*, 2024, **181**, 106628.
66 H. Gossler and O. Deutschmann, *Int. J. Hydrogen Energy*, 2015, **40**, 11046–11058.
67 S. Luo, L. Zeng, D. Xu, M. Kathe, E. Chung, N. Deshpande, L. Qin, A. Majumder, T. L. Hsieh, A. Tong, Z. Sun and L. S. Fan, *Energy Environ. Sci.*, 2014, **7**, 4104–4117.
68 BASF SE, *New technologies: Methane pyrolysis*, 2022, **https://www.basf.com/global/en/who-we-are/sustainability/we-produce-safely-and-efficiently/energy-and-climate-protection/carbon-management/innovations-for-a-climate-friendly-chemical-production.html#text-1002215085**. Access: August 4, 2024.
69 A. Holmen, O. Olsvik and O. A. Rokstad, *Fuel Process. Technol.*, 1995, **42**, 249–267.
70 F. G. Billaud, F. Baronnet and C. P. Gueret, *Ind. Eng. Chem. Res.*, 1993, **32**, 1549–1554.